crystals

MDPI

Article

Influence of Thermal Treatment on the Cross-Sectional Properties of Aerosol-Deposited $Pb(Mg_{1/3}Nb_{2/3})O_3-PbTiO_3$ Thick Films

Katarina Žiberna [1,2,*], Matej Šadl [1,2], Aljaž Drnovšek [3], Goran Dražić [1,2,4], Hana Uršič [1,2] and Andreja Benčan [1,2]

[1] Electronic Ceramics Department, Jožef Stefan Institute, Jamova Cesta 39, 1000 Ljubljana, Slovenia; matej.sadl@ijs.si (M.Š.); goran.drazic@ki.si (G.D.); hana.ursic@ijs.si (H.U.); andreja.bencan@ijs.si (A.B.)
[2] Jožef Stefan International Postgraduate School, Jamova Cesta 39, 1000 Ljubljana, Slovenia
[3] Department of Thin Films and Surfaces, Jožef Stefan Institute, Jamova Cesta 39, 1000 Ljubljana, Slovenia; aljaz.drnovsek@ijs.si
[4] Department of Materials Chemistry, National Institute of Chemistry, Hajdrihova 19, 1000 Ljubljana, Slovenia
* Correspondence: katarina.ziberna@ijs.si

Abstract: The thermal treatment of electromechanically active thick films prepared by aerosol deposition (AD) is a common practice to improve their electrical and electromechanical properties. We report on how post-deposition annealing in air affects the unique cross-sectional microstructure and mechanical properties of $0.9Pb(Mg_{1/3}Nb_{2/3})O_3-0.1PbTiO_3$ thick films prepared by AD. Transmission electron microscopy revealed minor but detectable changes, such as pore redistribution and grain growth after annealing at 500 °C. We also showed that the stainless-steel substrate is strongly affected by the annealing. The hardness and Young's modulus of the films increased after annealing, with both properties being discussed in terms of their distribution over the cross-sections of the films.

Keywords: aerosol deposition; thick films; microstructure; mechanical properties

Citation: Žiberna, K.; Šadl, M.; Drnovšek, A.; Dražić, G.; Uršič, H.; Benčan, A. Influence of Thermal Treatment on the Cross-Sectional Properties of Aerosol-Deposited $Pb(Mg_{1/3}Nb_{2/3})O_3-PbTiO_3$ Thick Films. *Crystals* **2023**, *13*, 536. https://doi.org/10.3390/cryst13030536

Academic Editor: Pavel Lukáč

Received: 22 February 2023
Revised: 17 March 2023
Accepted: 18 March 2023
Published: 21 March 2023

1. Introduction

Aerosol deposition (AD) is a method that enables the fabrication of high-density polycrystalline films at room temperature. The method was successfully used for preparing films for various applications, such as ferroelectric films for sensors and actuators, protective coatings, oxide ion-conductor layers in solid-oxide fuel cells, catalytic and superconductor layers [1,2]. The AD apparatus sprays submicron particles onto the substrate with high kinetic energy, and the film grows by impact consolidation and fracture of the initial powder particles [1,3,4]. Since the AD takes place at room temperature, a wide range of materials can be used as substrates, from metals with a low melting temperature [5–13] to ceramics [8,14,15], glass [8], and even polymers [16].

In some cases, a heat treatment is still required after the deposition to achieve the intended functionalities of the film. For example, additional annealing is essential for electromechanical films to improve dielectric, ferroelectric, and energy-storage properties [10–12,17–19]. The enhancement is thought to be related to the partial release of the residual stresses created in the films during deposition by the high-energy impacts [9,10,17,20]. For example, Khansur et al. reported a compressive stress in a $BaTiO_3$ film, measured by X-ray microdiffraction, that is not uniformly distributed across the film thickness. The peak stress of −800 MPa was measured near the film-substrate interface, and a significant decrease towards the surface was observed. Heat treatment at 500 °C reduced the total stress to −271 MPa, but the relaxation near the surface persisted [21]. At the same time, the annealing also affects the mechanical properties of these films. An increase in the hardness (H) and the Young's modulus (E) as well as a degradation in the plastic deformability and thus the crack resistance was observed after annealing [12,17], suggesting that an optimization

of the annealing temperature is required to achieve both the best electromechanical and mechanical properties of the AD films.

Studies of the mechanical properties of functional AD polycrystalline films are rare [7,12], mostly due to the experimental challenges related to the size of the film. The thickness of the film (up to few tens of μm) limits the application of most mechanical tests, leaving only the possibility of performing micro- and nano-mechanical tests, e.g., nanoindentation.

Here, we investigated the effects of heat treatment in air atmosphere on the cross-sectional mechanical properties of AD thick films using in-situ nanoindentation to gain a better understanding of the overall functional response of the films. The materials studied were aerosol-deposited $0.9Pb(Mg_{1/3}Nb_{2/3})O_3-0.1PbTiO_3$ (PMN−10PT) thick films on stainless steel, which showed a significant reduction in microstrains and an improvement in the energy-recovery density and energy-storage efficiency after heat treatment at 500 °C [10], but their mechanical behavior has not yet been investigated. In addition, we investigated the effects of heat treatment on the microstructure and composition throughout the film thickness, down to the nm range. We showed that the formation of nanopore-chain-like defects and grain growth are triggered when the film is annealed at 500 °C. The stresses created in the substrate by the impact of the powder particles during the deposition disappear after annealing, while the substrate oxidizes at the film-substrate interface. Although the microstructural changes appear to be minor, a non-negligible increase in the average *H* and *E* values was measured in the heat-treated film, with no cracking observed.

2. Materials and Methods

The $0.9Pb(Mg_{1/3}Nb_{2/3})O_3-0.1PbTiO_3$ (PMN−10PT) ceramic powder was synthesized by separately preparing the two end oxides from the initial powders, i.e., PbO (99.9%, Aldrich, St. Louis, MO, USA), MgO (99.95%, Alfa Aesar, Haverhill, MA, USA), TiO_2 (99.8%, Alfa Aesar, Haverhill, MA, USA) and Nb_2O_5 (99.9%, Aldrich, St. Louis, MO, USA). The prepared oxides, i.e., $Pb(Mg_{1/3}Nb_{2/3})O_3$ and $PbTiO_3$, were then mixed in the stoichiometric ratio and high-energy milled. Details of the procedure can be found elsewhere [10]. The high-energy-milled PMN−10PT powder was annealed at 900 °C for 1 h and then milled for 30 min with isopropanol using yttria-stabilized-zirconia milling balls with diameters of 3 mm at 200 min^{-1} to achieve the desired particle size and particle size distribution. Lastly, the powder was dried in a vacuum drier (10 mbar) at 100 °C for 12 h and sieved.

The substrate on which the film was deposited was a 15 mm × 15 mm stainless steel No. 304 (American Iron and Steel Institute, Washington, DC, USA) with a 0.8-mm thickness and a bright, polished surface (A480: No. 8, American Society for Testing and Materials, West Conshohocken, PA, USA). Prior to deposition, the stainless-steel substrates were cleaned with ethanol. The AD equipment was from InVerTec (Bayreuth, Germany). The deposition parameters are reported elsewhere [22].

Two films were prepared using the described procedure. One did not receive any further processing and is denoted in the text as as-deposited. The other film underwent a further heat treatment in air at 500 °C for 1 h with a heating and cooling rate of 2 K min^{-1} and is denoted in the text as annealed.

Scanning transmission electron microscopy (STEM) and transmission electron microscopy (TEM) were performed using a JEM 2100 (Jeol, Tokyo, Japan) and an ARM 200CF (Jeol, Tokyo, Japan) equipped with a Centurio 100-mm^2 SDD energy-dispersive X-ray spectroscopy system (EDS, Jeol, Tokyo, Japan), both operated at 200 kV. The 4D STEM data was obtained using a Merlin pixelated detector (Quantum Detectors, Oxford, UK). Samples for STEM/TEM were prepared by milling lamellae with a Ga^+-source focused ion beam (FIB) Helios Nanolab 650 HP (Thermo Fischer Scientific, Waltham, MA, USA). The volume percentage of defects in the FIB-prepared lamellae was estimated using Image J software (National Institute of Mental Health, Bethesda, MD, USA) [23].

The surface roughness was measured with a DektakXT Advanced System profilometer (Bruker, Billerica, MA, USA). Four line measurements of 2 mm each were performed on each sample and then averaged.

In-situ nanoindentation was performed with a Hysitron PI88 SEM PicoIndenter indentation system (Bruker, Billerica, MA, USA) inside a Quanta 650 ESEM (Thermo Fischer Scientific, Waltham, MA, USA). A force of 1 mN was applied over 5 s, held for 2 s and then released over 5 s. The hardness (H) and Young's modulus (E) of the films were determined using the methodology developed by Oliver and Pharr [24]. The Poisson's ratio (ν) used for the calculation of E was 0.3. This selection was made with the assumption that the ceramic PMN−10PT thick film had the same Poisson's ratio as the PMN ceramic [25]. A cube-corner diamond indentation probe with a nominal E = 1140 GPa and ν = 0.07 was used for indenting (Bruker, Billerica, MA, USA). The cross-sections of the two films on which the nanoindentation was performed were prepared by embedding the films in epoxy resin, grinding, and then polishing them with 9-µm, 6-µm, 3-µm, and $\frac{1}{4}$-µm diamond pastes. Fine polishing was achieved by polishing with a colloidal silica suspension for 15 h.

Scanning electron microscopy (SEM) after the nanoindentation was performed using a field-emission SEM Verios 4G HP (Thermo Fischer Scientific, Waltham, MA, USA) equipped with an EDS detector Aztec live, Ultim Max SSD 65 mm^2 from (Oxford Instruments, Abingdon, UK). Both imaging and EDS acquisition were performed at 15 keV. To avoid charging during the SEM analysis, the cross-sections of the films were coated with 5 nm of carbon using a Precise Etching and Coating System 628A (Gatan, Pleasanton, CA, USA).

Contact resonance frequency viscoelastic mappings (CRFMs) were made with a Jupiter XR atomic force microscope (Oxford Instruments Asylum Research, Santa Barbara, CA, USA) using AC160TS-R3 silicon tips with a nominal radius of 7 nm (Oxford Instruments Asylum Research, Santa Barbara, CA, USA).

3. Results and Discussion

3.1. Microstructure and Chemical Composition

First, we performed microstructural and compositional analyses of the cross-sections of both the as-deposited and the annealed ~6-µm-thick $0.9Pb(Mg_{1/3}Nb_{2/3})O_3-0.1PbTiO_3$ (PMN−10PT) films using scanning transmission electron microscopy (STEM). According to the X-ray diffraction (XRD) analysis, these films have a perovskite crystal structure (Figure S1) [10]. As shown in Figure 1 and Figure S2 (see Supplementary materials) both films have defects, i.e., some larger pores of 200 nm (marked by arrows in Figure 1a,c) and chain-like defects consisting of nanopores (marked by circles in Figure 1a,c). The volume percentage of defects is higher in the annealed film (1.1 vs. 0.6 %), indicating that the pores redistribute, and areas of lower local density are formed as the film is annealed. The roughness of the surface does not change significantly with annealing. The root-mean-square surface roughness of the as-deposited and the annealed films are (110 ± 10) nm and (105 ± 5) nm, respectively.

Energy-dispersive X-ray spectroscopy (EDS) mappings revealed a homogeneous distribution of all the elements across the cross-sections (Figure S3), with the exception of Mg (Figure 1b,d). Mg-rich nanosized impurities were found in both films. Similar inhomogeneities were observed in mechanochemically prepared PMN−10PT ceramics and identified as MgO, which due to its low reactivity remained unreacted during the mechanochemical reaction [26].

Next, we examined the region of the film near the substrate. Figure 2 shows the film-substrate interface (Figure 2a,c) and the elemental distribution of the main elements in the stainless-steel substrate, i.e., Fe, Cr, and Ni, at the film-substrate interface (Figure 2b,d) of the as-deposited film and the annealed film, respectively. As described above, the number of defects, i.e., nanoscale pores, is higher in the annealed film. In the as-deposited film we observed some brighter contrast at the interface (Figure 2a) extending about 500 nm into the substrate, indicating mechanical deformation of the substrate caused by the impact of the powder during deposition. Stresses in the substrate of the as-deposited film were also observed from the divergence map obtained from the 4D STEM data set

using differential phase contrast (Figure S4) that additionally revealed stresses of a higher magnitude localized at the film-substrate interface and around the defects in the film itself. According to the XRD studies, the internal stresses caused by particle impacts during the AD process on stainless-steel substrates are tensile stresses [8]. Stainless steel (hardness (*H)* of stainless steel No. 304 ~1.9 GPa [27]) is more susceptible to mechanical deformation than substrates with a higher *H*. For example, for $Pb(Zr_{0.52}Ti_{0.48})O_3$ deposited on Si, a 100−150-nm-layer damaged layer was reported for the substrate [6] (*H* of Si ~11.1 GPa [28]). The contrast caused by mechanical stresses is not seen in the substrate of the annealed film (Figure 2c), indicating that the stresses are relieved in the substrate during annealing.

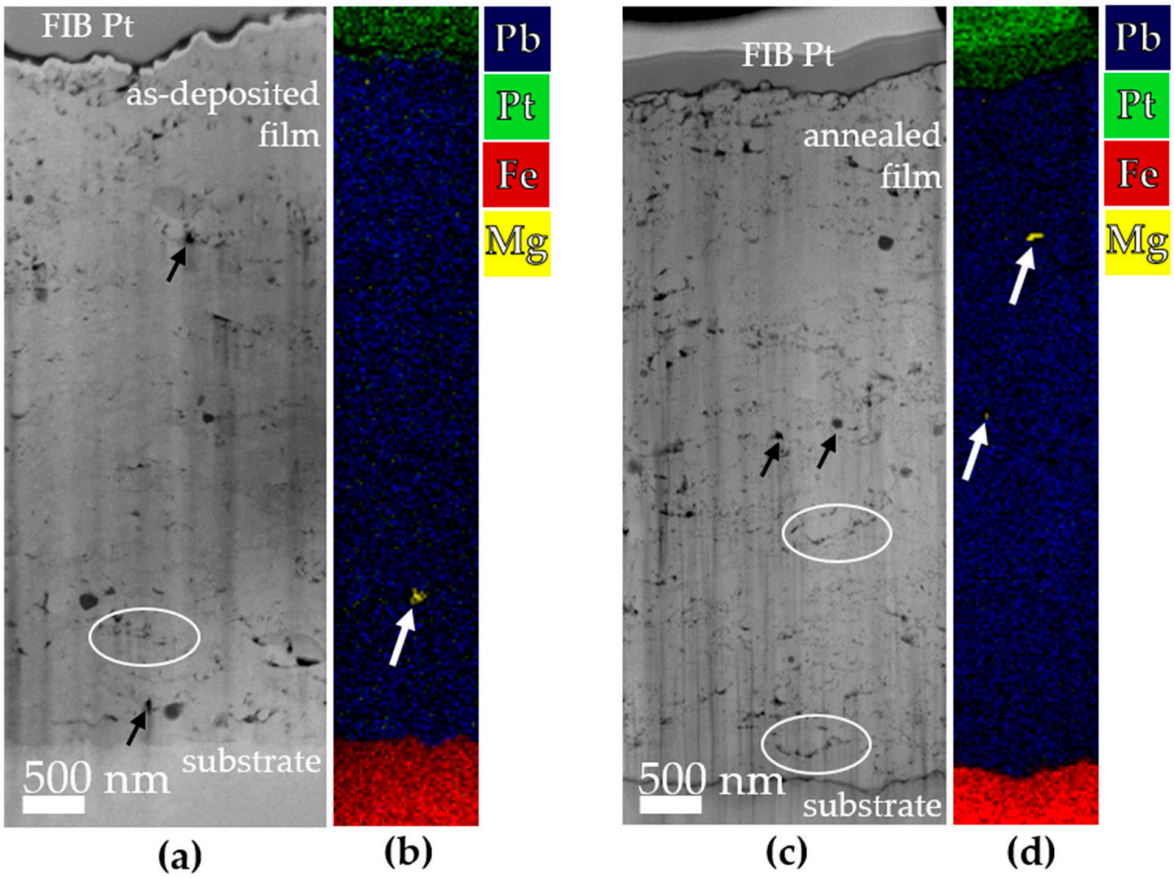

Figure 1. STEM dark-field and EDS analyses, respectively, of the (**a**,**b**) the as-deposited film and (**c**,**d**) the annealed PMN−10PT thick film. The black arrows on the STEM images (**a**,**c**) indicate larger pores in the films, while the circles mark the chain-like defects composed of nanopores. White arrows in the EDS mapping (**b**,**d**) mark Mg-rich inclusions in the films. Spectral lines Pb L, Pt M, Fe K, and Mg K were used for the EDS mapping.

In addition, a redistribution of the elements in the substrate occurs at the interface between the film and the substrate (Figure 2b,d). EDS showed that a layered structure is formed at the interface, which consists (from the substrate matrix to the film) of an Fe-rich and a Ni-rich layer, a Cr_xO_y layer, and an Fe_mO_n layer (Figure S5). Each layer is approximately 30−40-nm thick. Apart from the formation of the oxide layers, no reaction with the film was observed in the annealed sample. It is described in the literature that the passivation of stainless steel in air occurs at 300 °C due to the diffusivity of oxygen from the atmosphere into the substrate and metal ions towards the surface, forming a specific sequence of layers associated with the formation energies of Fe_mO_n, Cr_xO_y and NiO [29]. The source of oxygen forming the oxides in the substrate in our case has not been determined. However, there are some studies that support the claim that oxygen can diffuse through the film during annealing. Eckstein et al. argued that films deposited in an

oxygen-depleted carrier gas such as N_2, as used in this work, contain oxygen vacancies created during deposition that can serve as pathways for the oxygen, which presumably fills the vacancies during annealing in an oxygen-rich environment [13]. Another oxygen pathway through could be the grain boundaries, which have been reported to have a higher oxygen diffusivity than the grain matrix in nanocrystalline films [30]. The diffusion of oxygen might also be related to the redistribution of defects during annealing (Figure 1).

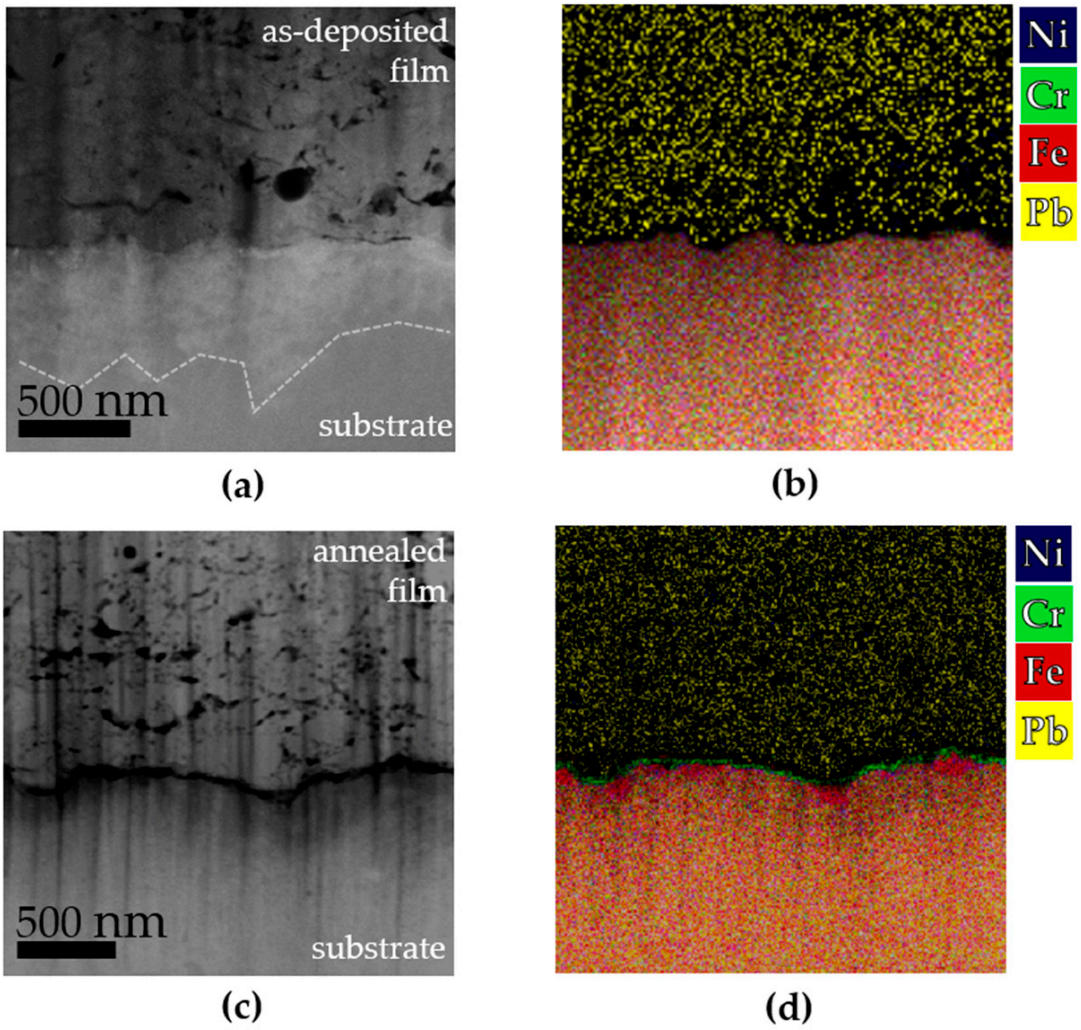

Figure 2. Film-substrate interface in STEM dark-field images and EDS, respectively, of (**a**,**b**) the as-deposited film and (**c**,**d**) the annealed film. In (**a**) the dashed line marks the extent of the mechanical deformation observed in the substrate due to particle impact. For the EDS mappings, the spectral lines Ni K, Cr K, Fe K and Pb L were used.

The influence of annealing on the grain size is shown in Figure 3. The as-deposited film consists of ~10 nm grains (Figure 3a), but the exact grain size is difficult to determine because the grains overlap. Annealing at 500 °C triggered grain growth (Figure 3b), with some grains growing up to about ~20 nm. The increase in grain size and crystallinity can also be observed from selected-area electron diffraction (SAED) recorded from larger areas of the FIB lamellae (Figure 3c), where more pronounced spots in diffraction rings are observed after annealing. The increase in grain size and better crystallinity after annealing affect the local stresses observed by XRD [10] and can contribute to improved electrical and electromechanical as well as mechanical properties of the heat-treated films.

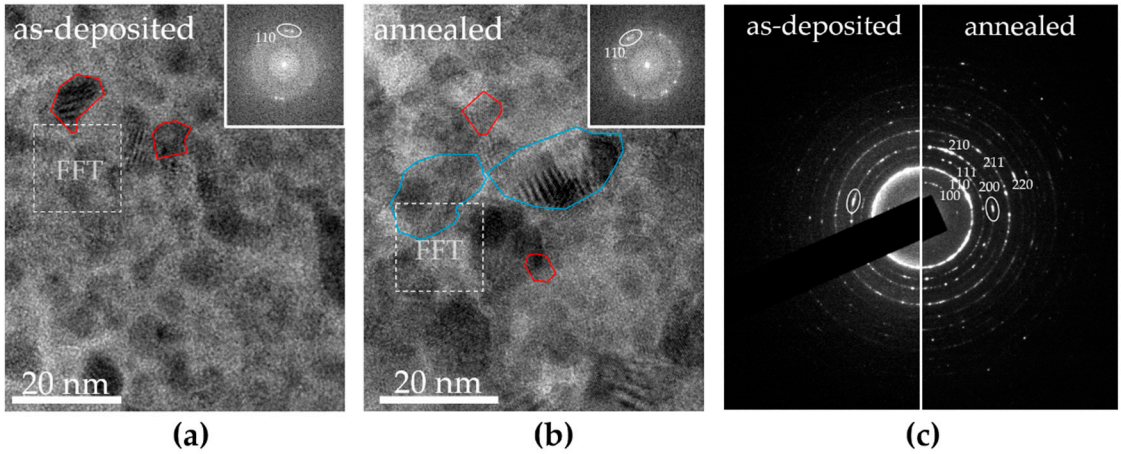

Figure 3. Transmission electron microscopy (TEM) images of grains in: (**a**) the as-deposited film with the FFT inset of the marked region; and (**b**) the annealed film (larger and smaller grains are circled in blue and red, respectively), with an inset of the FFT from the marked region. (**c**) Comparison of the SAED of both films. Circles mark reflections that are indicative of texturing. The $Pm\bar{3}m$ space group was used to index the SAED pattern (PDF#01-074-4513).

The proximity of the reflections in the SAED (some examples are circled in Figure 3c) indicates that the film has some texture. A fast Fourier transform (FFT) of selected regions in Figure 3a,b showed that the texture is very local and probably includes few neighboring grains. The local texturing is a result of deposition causing the larger particles to break upon impact. On a TiO_2 nanoparticle model system, Daneshian et al. predicted, using molecular dynamics, that a particle deposited by AD will fragment after impact and the fragmented parts will form low-angle grain boundaries [31]. Other authors also reported a reorientation of the crystallites during annealing at 500 °C in $BaTiO_3$ [12], which was not observed in our case, at least not to affect and thus reduce the local texturing after annealing.

3.2. Mechanical Behavior

Finally, the mechanical properties of the films were investigated by nanoindentation over cross-sections. A matrix of nanoindentations was made for each film, as shown in Figure 4a,b. At an applied load of 1 mN, both films exhibited good ductility as no cracks were observed around the indentations in either film. Zhuo et al. showed for $BaTiO_3$ that a threshold load of 200 g (~2 N) is required to see the difference in the crack resistance between the as-deposited and annealed films, with the as-deposited films performing better and not forming cracks around the indentations [12]. The crack resistance of the films, which is not characteristic of conventionally sintered ceramics [32], is probably related to the high density of the grain boundaries, which makes it easy for the grains to slide against each other during indentation, as well as to other defects in the films, such as dislocations [13].

The differences in the mechanical properties of the films can be seen from the force-depth curves in Figure 4c,d. The curves of the as-deposited film (Figure 4c) are more uniform, while the curves of the annealed film show a larger scatter and many pop-ins (sudden jumps of the measured depth at a constant force) are observed in the loading portions of the curves. The difference can be attributed to the change in microstructural properties, i.e., redistribution of the pores (Figure 1) and grain growth (Figure 3) observed after annealing. The overall increase in H and Young's modulus (E) of the AD films after annealing from (5.9 ± 0.3) GPa to (6.8 ± 0.6) GPa and from (107.6 ± 7.7) GPa to (125.5 ± 9.3) GPa, respectively, is in the literature associated with relaxation of residual stresses [12,17]. The increase in the standard deviation of H and E also reflects the changes in the microstructure caused by the heat treatment.

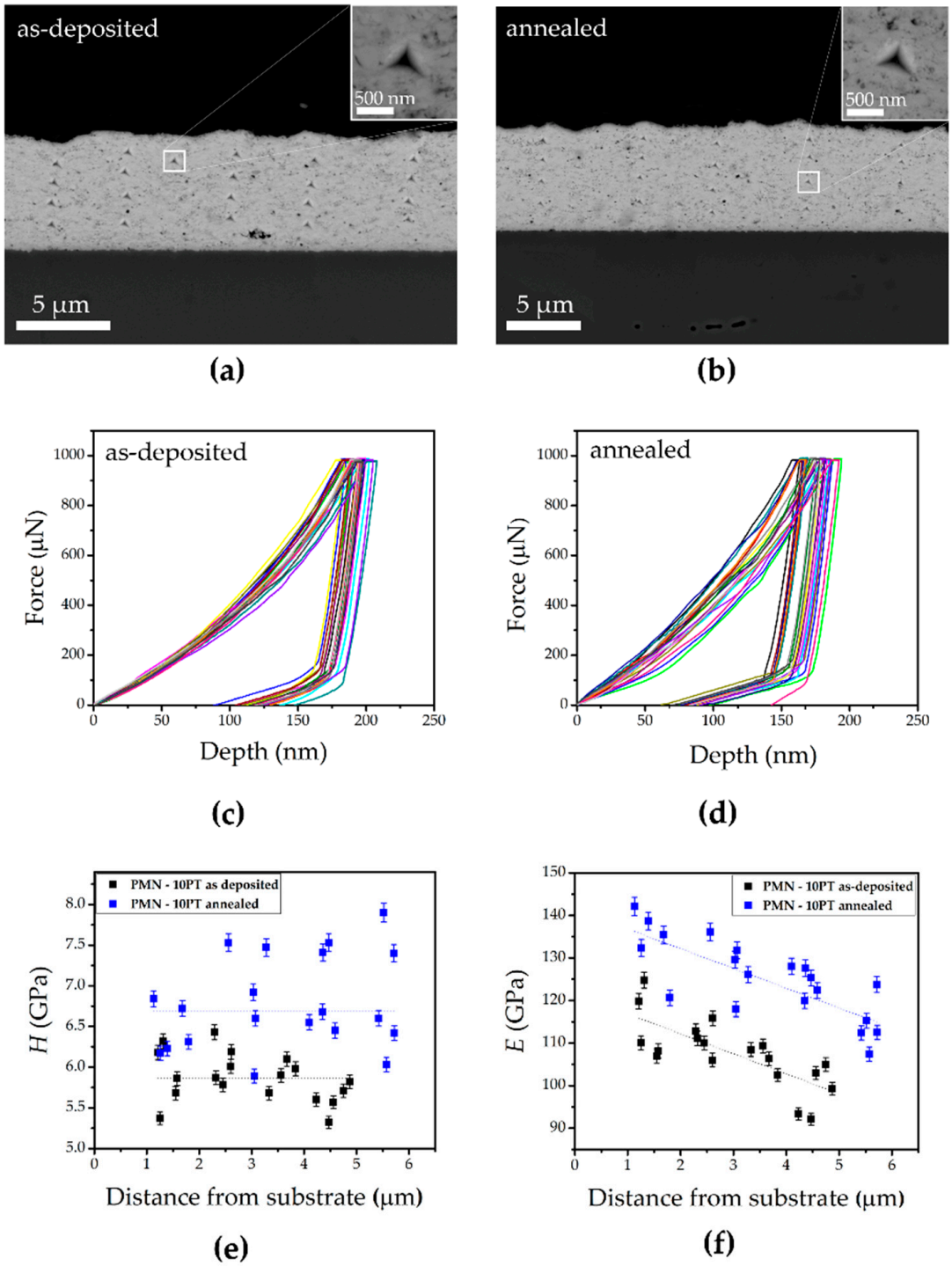

Figure 4. SEM images of indents made on cross-sections of (**a**) the as-deposited and (**b**) annealed film. Force-depth curves of (**c**) the as-deposited and (**d**) annealed film. (**e**) Hardness calculated from individual measurements plotted against indentation position for both films. (**f**) Young's modulus calculated from individual measurements, plotted against the position of the indentation for both films. The error bars represent the uncertainty of the method as determined from measurements on the fused-silica standard. The dashed lines serve only as a guide to the eyes.

In Figure 4e,f the calculated values of H and E, respectively, from the individual indentations are plotted as a function of position relative to the film-substrate interface. H (Figure 4e) shows no specific trend across the film thickness and no influence of the substrate on the measurement was observed (H of stainless steel No. 304 ~1.9 GPa [27]). The same cannot be said for E (Figure 4f). For both films, E decreases linearly as the surface is approached, which is a consequence of the elastic properties of the substrate being measured with those of the film. The E of the substrate is higher than that of the film, as confirmed by the contact resonance frequency maps, (Figure S6) (E of stainless steel No. 304 ~200 GPa [27]). The influence of the substrate is strongest near the film-substrate interface, so a higher E is measured, and appears to have a significant range of at least 5 µm. Measuring E by nanoindentation across the cross-section of films can be challenging due to the large elastic zone that is deformed under the indentation probe [33]. The oxides that form at the interface between the film and the substrate are likely to contribute little to the total E measured.

4. Conclusions

The microstructure of $0.9Pb(Mg_{1/3}Nb_{2/3})O_3-0.1PbTiO_3$ thick films deposited on stainless steel by aerosol deposition (AD) was studied before and after annealing in air at 500 °C to determine the changes in the unique microstructure created by the AD process. The changes appear to be small, but detectable, such as the redistribution of pores into chain-like defects consisting of nanopores and grain growth after heat treatment. Local texturing at the level of a few adjacent grains was also observed in both films. Interestingly, annealing affects the substrate as well by relieving stresses caused by the impact of particles during the AD process and the oxidation of the substrate at the film-substrate interface.

While annealing induced microstructural changes at the nanoscale, the mechanical properties, i.e., the hardness and Young's modulus, were significantly affected, as evidenced by the increase in both values after annealing. Both films resisted cracking at a force of 1 mN, which is not observed in conventionally produced ceramics, and is a consequence of the unique microstructure of the densely packed nanograins produced by the AD method.

Supplementary Materials: The following supporting information can be downloaded at: https://www.mdpi.com/article/10.3390/cryst13030536/s1, Figure S1: X-ray diffraction patterns of the as deposited and the annealed film. All peaks were indexed with a cubic perovskite structure (space group $Pm\bar{3}m$, JCPDS 81-0861) Figure S2: Scanning transmission electron microscopy (STEM) (a) dark-field and (b) bright-field images of the as-deposited film; (c) the dark-field and (d) bright-field images of the annealed film. Note that the black and white arrows point to pores locations, which are black in dark field and white in bright field. The vertical lines observed on the STEM images are a consequence of the focused ion beam curtain effect; Figure S3: Compositional analysis of the as deposited and the annealed film, respectively, performed using (a) and (b) EDS-STEM and (c) and (d) EDS-SEM with the corresponding EDS line analysis. The white arrows in (a) and (b) indicate the Mg-rich inclusions; Figure S4: (a) STEM dark-field image of the film-substrate interface in the as-deposited film; (b) the corresponding divergence map obtained from the 4D STEM dataset using differential phase contrast. Areas with higher contrast in the divergence map represent higher local strain; Figure S5: EDS of the film-substrate interface of the annealed PMN−10PT thick film resolving a layered structure formed due to oxidation of the substrate at 500 °C. The layer structure is composed (from substrate to film) of an Fe- and Ni-rich layer, a Cr_xO_y layer and an Fe_mO_n layer; Figure S6: (a) Topography and (b) frequency mapping at the film-substrate interface of the as-deposited film measured in the contact resonance frequency viscoelastic mapping mode. This is an atomic force microscopy technique in which the frequency measured is the resonant frequency of the tip-material system and is related to the Young's modulus of the material. The higher the frequency, the higher the Young's modulus and vice versa. In b, a higher frequency is measured in the substrate than in the film, which means that the substrate has a higher Young's modulus than the film.

Author Contributions: K.Ž. and A.B. designed the experiments. M.Š. and H.U. prepared the thick-film samples. K.Ž. and A.D. performed the in-situ nanoindentation. K.Ž. performed the SEM analysis and CRFM measurements. K.Ž., A.B. and G.D. performed the TEM analysis. K.Ž. and A.B. wrote the manuscript. All authors revised and edited the manuscript. A.B. supervised the project. All authors have read and agreed to the published version of the manuscript.

Funding: This work is funded by the Slovenian Research Agency in the frame of national postgraduate funding (K. Ž.), core funding P2-0105 and projects J7-4637, J2-3041, J2-3058, J2-2497 and I0-0005.

Data Availability Statement: Not applicable.

Acknowledgments: Jena Cilenšek is acknowledged for her help in preparing the samples for nanoindentation. Val Fišinger is acknowledged for helping with atomic force microscopy. JSI Director's fund 2017-ULTRACOOL project is also acknowledged.

Conflicts of Interest: The authors declare no conflict of interest.

References

1. Hanft, D.; Exner, J.; Schubert, M.; Stöcker, T.; Fuierer, P.; Moos, R. An Overview of the Aerosol Deposition Method: Process Fundamentals and New Trends in Materials Applications. *J. Ceram. Sci. Technol.* **2015**, *6*, 147–181. [CrossRef]
2. Schubert, M.; Hanft, D.; Nazarenus, T.; Exner, J.; Nieke, P.; Glosse, P.; Leupold, N.; Kita, J.; Moos, R. Powder Aerosol Deposition Method—Novel Applications in the Field of Sensing and Energy Technology. *Funct. Mater. Lett.* **2019**, *12*, 1930005. [CrossRef]
3. Akedo, J. Room Temperature Impact Consolidation (RTIC) of Fine Ceramic Powder by Aerosol Deposition Method and Applications to Microdevices. *J. Therm. Spray Technol.* **2008**, *17*, 181–198. [CrossRef]
4. Saunders, R.; Johnson, S.D.; Schwer, D.; Patterson, E.A.; Ryou, H.; Gorzkowski, E.P. A Self-Consistent Scheme for Understanding Particle Impact and Adhesion in the Aerosol Deposition Process. *J. Therm. Spray Technol.* **2021**, *30*, 523–541. [CrossRef]
5. Akedo, J.; Lebedev, M. Piezoelectric Properties and Poling Effect of Pb(Zr, Ti)O_3 Thick Films Prepared for Microactuators by Aerosol Deposition. *Appl. Phys. Lett.* **2000**, *77*, 1710–1712. [CrossRef]
6. Akedo, J.; Lebedev, M. Microstructure and Electrical Properties of Lead Zirconate Titanate (Pb(Zr_{52}/Ti_{48})O_3) Thick Films Deposited by Aerosol Deposition Method. *Jpn. J. Appl. Phys.* **1999**, *38*, 5397–5401. [CrossRef]
7. Kim, H.K.; Oh, J.M.; Kim, S.I.; Kim, H.J.; Lee, C.W.; Nam, S.M. Relation between Electrical Properties of Aerosol-Deposited $BaTiO_3$ Thin Films and Their Mechanical Hardness Measured by Nano-Indentation. *Nanoscale Res. Lett.* **2012**, *7*, 1–16. [CrossRef]
8. Khansur, N.H.; Eckstein, U.; Li, Y.; Hall, D.A.; Kaschta, J.; Webber, K.G. Revealing the Effects of Aerosol Deposition on the Substrate-Film Interface Using NaCl Coating. *J. Am. Ceram. Soc.* **2019**, *102*, 5763–5771. [CrossRef]
9. Khansur, N.H.; Eckstein, U.; Benker, L.; Deisinger, U.; Merle, B.; Webber, K.G. Room Temperature Deposition of Functional Ceramic Films on Low-Cost Metal Substrate. *Ceram. Int.* **2018**, *44*, 16295–16301. [CrossRef]
10. Sadl, M.; Condurache, O.; Bencan, A.; Dragomir, M.; Prah, U.; Malic, B.; Deluca, M.; Eckstein, U.; Hausmann, D.; Khansur, N.H.; et al. Energy-Storage-Efficient 0.9Pb($Mg_{1/3}Nb_{2/3}$)O_3–0.1$PbTiO_3$ Thick Films Integrated Directly onto Stainless Steel. *Acta Mater.* **2021**, *221*, 117403. [CrossRef]
11. Sadl, M.; Nadaud, K.; Bah, M.; Levassort, F.; Eckstein, U.; Khansur, N.H.; Webber, K.G.; Ursic, H. Multifunctional Energy Storage and Piezoelectric Properties of 0.65Pb($Mg_{1/3}Nb_{2/3}$)O_3-0.35$PbTiO_3$ thick Films on Stainless-Steel Substrates. *J. Phys. Energy* **2022**, *4*, 024004. [CrossRef]
12. Zhuo, F.; Eckstein, U.R.; Khansur, N.H.; Dietz, C.; Urushihara, D.; Asaka, T.; Kakimoto, K.I.; Webber, K.G.; Fang, X.; Rödel, J. Temperature-Induced Changes of the Electrical and Mechanical Properties of Aerosol-Deposited $BaTiO_3$ Thick Films for Energy Storage Applications. *J. Am. Ceram. Soc.* **2022**, *105*, 4108–4121. [CrossRef]
13. Eckstein, U.; Exner, J.; Bencan Golob, A.; Ziberna, K.; Drazic, G.; Ursic, H.; Wittkämper, H.; Papp, C.; Kita, J.; Moos, R.; et al. Temperature-Dependent Dielectric Anomalies in Powder Aerosol Deposited Ferroelectric Ceramic Films. *J. Mater.* **2022**, *8*, 1239–1250. [CrossRef]
14. Suzuki, M.; Akedo, J. Temperature Dependence of Dielectric Properties of Barium Titanate Ceramic Films Prepared by Aerosol Deposition Method. *Jpn. J. Appl. Phys.* **2010**, *49*, 09MA10. [CrossRef]
15. Khansur, N.H.; Eckstein, U.; Uršič, H.; Sadl, M.; Brehl, M.; Martin, A.; Riess, K.; de Ligny, D.; Webber, K.G. Enhanced Electromechanical Response and Thermal Stability of 0.93($Na_{1/2}Bi_{1/2}$)TiO_3-0.07$BaTiO_3$ Through Aerosol Deposition of Base Metal Electrodes. *Adv. Mater. Interfaces* **2021**, *8*, 2100309. [CrossRef]
16. Sadl, M.; Lebar, A.; Valentincic, J.; Ursic, H. Flexible Energy-Storage Ceramic Thick-Film Structures with High Flexural Fatigue Endurance. *ACS Appl. Energy Mater.* **2022**, *5*, 6896–6902. [CrossRef]
17. Maruyama, K.; Kawakami, Y.; Narita, F. Young's Modulus and Ferroelectric Property of $BaTiO_3$ Films Formed by Aerosol Deposition in Consideration of Residual Stress and Film Thickness. *Jpn. J. Appl. Phys.* **2022**, *61*, SN1011. [CrossRef]
18. Nadaud, K.; Sadl, M.; Bah, M.; Levassort, F.; Ursic, H. Effect of Thermal Annealing on Dielectric and Ferroelectric Properties of Aerosol-Deposited 0.65Pb($Mg_{1/3}Nb_{2/3}$)O_3-0.35$PbTiO_3$ thick Films. *Appl. Phys. Lett.* **2022**, *120*, 112902. [CrossRef]
19. Ryu, J.; Choi, J.J.; Hahn, B.D.; Park, D.S.; Yoon, W.H. Ferroelectric and Piezoelectric Properties of 0.948($K_{0.5}Na_{0.5}$)NbO_3−0.052$LiSbO_3$ Lead-Free Piezoelectric Thick Film by Aerosol Deposition. *Appl. Phys. Lett.* **2008**, *92*, 2006–2009. [CrossRef]

20. Hoshina, T.; Furuta, T.; Kigoshi, Y.; Hatta, S.; Horiuchi, N.; Takeda, H.; Tsurumi, T. Size Effect of Nanograined $BaTiO_3$ Ceramics Fabricated by Aerosol Deposition Method. *Jpn. J. Appl. Phys.* **2010**, *49*, 03MC02. [CrossRef]
21. Khansur, N.H.; Eckstein, U.; Riess, K.; Martin, A.; Drnec, J.; Deisinger, U.; Webber, K.G. Synchrotron X-ray Microdiffraction Study of Residual Stresses in $BaTiO_3$ Films Deposited at Room Temperature by Aerosol Deposition. *Scr. Mater.* **2018**, *157*, 86–89. [CrossRef]
22. Sadl, M.; Tomc, U.; Prah, U.; Ursic, H. Protective Alumina Coatings Prepared by Aerosol Deposition on Magnetocaloric Gadolinium Elements. *Inf. MIDEM* **2019**, *49*, 177–182. [CrossRef]
23. ImageJ. Available online: https://imagej.net/ij/ (accessed on 27 December 2022).
24. Oliver, W.C.; Phaar, G.M. An Improvved Techniques for Determining Hardness and Elastic Modulus Using Using Load and Dispacement Sensing Indentation Experiments. *J. Mater. Res.* **1992**, *7*, 1564–1583. [CrossRef]
25. Catalan, G.; Corbett, M.H.; Bowman, R.M.; Gregg, J.M. Effect of Thermal Expansion Mismatch on the Dielectric Peak Temperature of Thin Film Relaxors. *J. Appl. Phys.* **2002**, *91*, 2295–2301. [CrossRef]
26. Uršič, H.; Vrabelj, M.; Otoničar, M.; Furlanović, L.; Rožič, B.; Kutnjak, Z.; Bobnar, V.; Malič, B. Influence of Synthesis-Related Microstructural Features on the Electrocaloric Effect for $0.9Pb(Mg_{1/3}Nb_{2/3})O_3$–$0.1PbTiO_3$ Ceramics. *Crystals* **2021**, *11*, 372. [CrossRef]
27. Stainless Steel—Grade 304 (UNS S30400). Available online: https://www.azom.com/properties.aspx?ArticleID=965 (accessed on 13 January 2023).
28. Walls, M.G.; Chaudhri, M.M.; Tang, T.B. Stm Profilometry of Low-Load Vickers Indentations in a Silicon Crystal. *J. Phys. D Appl. Phys.* **1992**, *25*, 500–507. [CrossRef]
29. Devaraj, A.; Barton, D.J.; Li, C.H.; Lambeets, S.V.; Liu, T.; Battu, A.; Vaithiyalingam, S.; Thevuthasan, S.; Yang, F.; Guo, J.; et al. Visualizing the Nanoscale Oxygen and Cation Transport Mechanisms during the Early Stages of Oxidation of Fe–Cr–Ni Alloy Using In Situ Atom Probe Tomography. *Adv. Mater. Interfaces* **2022**, *9*, 2200134. [CrossRef]
30. Navickas, E.; Huber, T.M.; Chen, Y.; Hetaba, W.; Holzlechner, G.; Rupp, G.; Stöger-Pollach, M.; Friedbacher, G.; Hutter, H.; Yildiz, B.; et al. Fast Oxygen Exchange and Diffusion Kinetics of Grain Boundaries in Sr-Doped $LaMnO_3$ Thin Films. *Phys. Chem. Chem. Phys.* **2015**, *17*, 7659–7669. [CrossRef]
31. Daneshian, B.; Gärtner, F.; Assadi, H.; Vidaller, M.V.; Höche, D.; Klassen, T. Features of Ceramic Nanoparticle Deformation in Aerosol Deposition Explored by Molecular Dynamics Simulation. *Surf. Coat. Technol.* **2022**, *429*, 127886. [CrossRef]
32. Porz, L.; Klomp, A.J.; Fang, X.; Li, N.; Yildirim, C.; Detlefs, C.; Bruder, E.; Höfling, M.; Rheinheimer, W.; Patterson, E.A.; et al. Dislocation-Toughened Ceramics. *Mater. Horiz.* **2021**, *8*, 1528–1537. [CrossRef]
33. Zak, S.; Trost, C.O.W.; Kreiml, P.; Cordill, M.J. Accurate Measurement of Thin Film Mechanical Properties Using Nanoindentation. *J. Mater. Res.* **2022**, *37*, 1373–1389. [CrossRef]